Solid-State Materials for Hydrogen Storage **15**

Rolando Pedicini, Irene Gatto, and Enza Passalacqua

Contents

R. Pedicini (✉)
Institute for Advanced Energy Technologies, Messina, Italy

Dipartimento di Fisica, Università della Calabria, Arcavacata di Rende, CS, Italy
e-mail: rolando.pedicini@itae.cnr.it

I. Gatto · E. Passalacqua
Institute for Advanced Energy Technologies, Messina, Italy

Abstract

Hydrogen (H_2) is a promising replacement energy carrier and storage molecular due to its high energy density by weight. For the constraint of size and weight in vehicles, the onboard hydrogen storage system has to be small and lightweight. Therefore, a lot of research is devoted to finding an efficient method of hydrogen storage based on both mechanical compression and sorption on solid-state materials. An overview of the current research trend and perspectives on materials-based hydrogen storage including both physical and chemical storage is provided in the present paper. Part of this chapter was dedicated to recent results on two innovative materials: hybrid materials based on manganese oxide anchored to a polymeric matrix and natural volcanic powders. A prototype H_2 tank, filled with the developed hybrid material, was realized and integrated into a polymer electrolyte membrane (PEM) single fuel cell (FC) demonstrating the material capability to coupling with the FC.

15.1 Introduction

The need for an alternative to fossil fuels is escalating due to the increasing problem of global warming and climate change, not to mention worries over energy security and adverse health effects [1].

New alternative energy sources are required to replace fossil fuels, for example, by using energy generated from the wind and/or solar energy. One of the actively explored concepts is to convert solar energy directly to hydrogen and then to use hydrogen as an energy carrier and a fuel for, e.g., cars. Considering that water covers about 71% of the earth's surface, we have almost an unlimited source of hydrogen. Hydrogen has an extremely high gravimetrical energy density (142 MJ kg^{-1}), which is at least three times larger than the equivalent value for liquid hydrocarbons (47 MJ kg^{-1}). Hydrogen as the fuel is also environmentally friendly as the only exhaust product in both combustion and fuel cell engines is water vapor. Therefore, hydrogen is an attractive candidate for replacement of petrol or diesel in cars or other vehicles.

Hydrogen can be used as a fuel in cars with slightly modified combustion engines. However, combustion engines are not a sustainable solution due to the relatively low efficiency (fuel for useful work ratio) of ~25%. On another hand, cars can be powered by fuel cells (FCs), electrochemical devices, which combine hydrogen and oxygen to produce electricity. Fuel cells convert hydrogen into electricity with an efficiency of 50–60% and release only water and heat as side products. The main obstacle for widespread application of FCs is the absence of sufficiently good and compact, lightweight hydrogen storage systems which are capable of delivering hydrogen gas to an FC at nearly room temperature and at pressures not much higher than atmospheric pressure. An average modern car equipped with a combustion engine needs approximately 30–35 l of petrol or diesel to travel 500 km, and the

combined weight of the fuel and the tank is about 80 kg. A car equipped with an FC engine would need about 5 kg of hydrogen to travel the same distance. The problem is that 5 kg of hydrogen at normal conditions (room temperature and atmospheric pressure) occupy ~56,000 l of space which is equivalent to a balloon of the diameter of 5 m. In this contest, the storage of hydrogen is identified as one of the major problems to be solved in the short and medium terms.

In a hydrogen storage system, aspects such as safety, reversible hydrogen uptake and the release rate, cost, weight, and volume must also be taken into account. According to multi-annual work plan (2014–2020) of *Fuel Cells and Hydrogen Joint Undertaking* (FCH JU) group under The *Horizon* 2020 program [2], the targets for hydrogen storage for transportation are 600 euros-per-kilogram-hydrogen (€/Kg H_2) for system cost and 0.023 Kg $\times$ L^{-1} and 5 wt.% of the volumetric and gravimetric capacity of H_2 tank system, respectively.

There are three possible ways in which hydrogen can be stored: gas compression, liquefaction, and storage within solid-state materials. Compressed gas is currently the most common form of hydrogen storage. Typically, tanks are made from steel and used at an operating pressure from 200 to 350 bar. However, lightweight composite cylinders have operating pressures up to 800 bar, where hydrogen has a volumetric density of 36 kg $\times$ m^{-3}. The amount of energy used to compress hydrogen gas depends on what pressure it is being compressed from and to, as well as the method using the gas compression. The ideal (isothermal, $\Delta T = 0$) compression of hydrogen from 1 to 800 bar requires 2.21 kWh $\times$ kg^{-1} of energy, which is ca. 5% of the energy content in hydrogen. In a real process, the work consumption is significantly higher because compression is not isothermal. In fact, adiabatic compression ($V^\gamma P$ = constant, where γ is the adiabatic exponent) requires over 16% of the energy content in hydrogen.

Liquid hydrogen must be stored below its low critical temperature (33 K) and pressure (13 bar); typically it is stored at its boiling point (20.3 K). The volumetric density of liquid hydrogen is 70.8 kg m^{-3} almost twice that of compressed hydrogen gas. The significant disadvantages of storing hydrogen as a liquid are boil-off and the relatively large amount of energy required for the liquefaction (30% of the lower heating value). However, boil-off losses are reduced when large-scale storage vessels are used due to the small surface-to-volume ratio, as the evaporation rate decreases as the size of the storage tank increases.

The hydrogen storage by solid-state materials has definite advantages from a safety perspective. Extensive efforts have been made on new hydrogen storage systems, including metal-organic frameworks (MOFs), zeolites, metal hydrides (MH), metal nitrides ($M_x N_2$), metal imides (MNR), doped polymers, hollow glass microspheres, and carbon-based materials. In solid-state storage, hydrogen is bonded by either physical, e.g., MOF and carbon-based materials, or chemical forces, e.g., hydrides, imides, and nitrides. Physisorption has the advantages of higher energy efficiency and faster adsorption/desorption cycles, whereas chemisorption results in the adsorption of larger amounts of gas but, in some cases, is not reversible and requires a higher temperature to release the adsorbed gas.

15.2   Physisorption

The large surface areas of porous materials, especially of nanostructures, allow the adsorption of large quantities of hydrogen; for this reason, the use of porous materials and their simplicity of physisorption attract scientific interests. Two fundamental parameters have to be taken into account for optimal hydrogen storage: the average surface available per unit volume of the adsorbent and the characteristic binding energy of the hydrogen molecule with the material. Physisorption involves weak van der Waals forces, and this weak physisorption interaction requires cryogenic temperatures (typically 77 K) and high pressure to reach reasonable hydrogen storage values. Porous carbonaceous materials have been identified to be attractive for hydrogen storage. Experimental and theoretical studies have shown that the interaction energies between H_2 and pure carbon materials are in the range from 4 kJ mol^{-1} for activated carbon and graphite to 15 kJ·mol^{-1} for internal and interstitial sites of single-walled nanotubes (SWNTs), very low for storing large amounts of hydrogen at room temperature and relatively low pressures. Optimal interaction energies should be over 100 kJ·mol^{-1}.

Since the first studies [3], carbon nanotubes (CNTs), single-walled and multi-walled carbon nanotubes (SWNTs and MWNT), have been investigated extensively as potential hydrogen storage materials because of their low density, wide variety of structural forms, extensive pore structure, good chemical stability, and the ability to modify the structures using wide range of preparation, carbonization, and activation condition. Many of the reported results are controversial, with H_2 sorption that varies from less than 0.1 wt.% to more than 10 wt.% depending on measurement method and operating conditions. High values were obtained in cryogenic conditions unsuitable for mobile applications; when ambient conditions are used, this value is less than 1 wt.% [4].

To improve the hydrogen sorption properties of carbon materials, a chemical activation has been proposed. Activated carbons (AC) produced using potassium hydroxide [KOH] as an activating agent exhibit high surface areas, large pore volumes, and uniform micropore-size distributions suitable for hydrogen sorption. In particular, AC with a two-step procedure in which physical activation (with carbon dioxide [CO_2]) was followed by a chemical (KOH) activation step exhibited a hydrogen adsorption capacity up to 7.08 wt.% at 469 K and 2 MPa H_2 pressure [5]. Changes in hydrogen uptakes of porous carbons were found with nitrogen incorporation into carbon. Starting from hydrothermally carbonized chitosan and successive activation with KOH, a hydrogen storage at 77 K of 1.75–2.71 wt.% and 4.23–6.77 wt.% at 1 bar and 20 bar was, respectively, obtained [6].

Among carbon materials for hydrogen storage, graphene recently was cited as a promising adsorbent material due to its high surface area up to 2630 m^2 g^{-1}, but H_2 uptake for bulk graphene-related materials evaluated at ambient temperature and 77 K does not exhibit superior hydrogen storage (generally less than 1 wt.% at room temperature and 120 bar) compared to other nanostructured carbon materials like activated carbons, CNTs, or nano-fiber. The use of transition metals to obtain decorated graphene has been proposed, to increase the hydrogen storage capacity

through a spillover mechanism at ambient conditions. Recent results report a highly enhanced hydrogen storage capacity (3.19 wt.%) under a practical operating condition of 298 K at 100 bar for a bioinspired graphene foam based on polydopamine (PD, -[$C_8H_5NO_2$]$_p$ - [$C_8H_7NO_2$]$_o$ - [$C_8H_9NO_2$]$_n$ - [$C_8H_{11}NO_2$]$_m$-, where p, o, n, and m represent the monomers) and decorated with Pt nanoparticles shown [7].

Another efficient approach for the fabrication of porous carbon materials is the template carbonization method, which allows obtaining materials with controlled physical and chemical properties. Among them, zeolites, $\left[M_{\frac{x}{n}}\left[(AlO_2)_x(SiO_2)_y\right]\cdot_mH_2O\right]$, where M is the ion balancing the charge of the aluminosilicate ion, are attractive due to their versatility and three-dimensional pore channels. A large number of zeolites with a variety of pore structures have been used, and it has been reported that zeolites can store up to 4.5 wt.% of hydrogen at 35 K and 0.96 MPa and 1.81 wt.% at 77 K and 1.5 MPa. Several modifications were carried out to improve the H_2 capacity, such as a combined liquid impregnation/chemical vapor deposition (CVD) process on a commercially available zeolite as a hard template to produce a porous carbon with hydrogen uptake capacities in the range of 3.4–6.3 wt.% (at 77 K and 20 bar).

Metal-organic frameworks (MOFs) could be considered an interesting candidate for hydrogen storage due to their high crystallinity, purity, porosity, and tunable structural characteristics. The MOF's interconnections provide an ordered network of channels or pores wherein molecular H_2 can be reversibly captured and released. An MOF is an interconnect structure which mainly consists of an organic linker and a metal cluster with high surface area and is typically only available in the form of loose powders, which can be problematic to incorporate into the relevant device structures. In 2003, the initial H_2 storage data were reported for *isoreticular metal-organic framework-1* (IRMOF-1, also known as MOF-5) (4.5 wt.% at 77 K and 1 atm), which were prepared from benzene-1,4-dicarboxylate (BDC) and Zn(II) salt. The structure consists of Zn_4 O nodes with BDC linkages between the nodes [8].

To increase the surface area, a multi-ligand strategy was used for porous *University of Michigan Crystalline Material-2* (UMCM-2) MOF of the surface area of 5200 m^2 g^{-1}, consisting of Zn_4 O metal clusters linked together by two linear dicarboxylates and four trigonal planar ligands arranged in an octahedral geometry with a hydrogen capacity of 6.9 wt. at 77 K and 4.6 MPa [9]. Other studies have reported a mesoporous *Technical University of Denmark-6* (DTU-6) MOF using a secondary linker to stabilize a highly open framework structure, leading to an H_2 uptake of 5.64 wt.% at 77 K and 5 MPa.

Chromium-based metal-organic framework (Cr-MOF) has been explored as potential material, and to lower the production cost waste, polyethylene terephthalate (PET) bottles were used as a source of terephthalic acid (BDC) linker for the synthesis. The PET-derived Cr-MOF materials showed a 2.1 wt.% of H_2 adsorption at 77 K and 1 bar higher than commercial-derived in the same conditions (1.8 wt.%).

Improvements in H_2 adsorption of Cr-based MOF were obtained from a hybrid composite of zeolite template carbon (ZTC) and Cr-based *Matérial Institut Lavoisier-101* (MIL-101) MOF. The hydrogen uptake capacities of individual MIL-101 and zeolite template carbon (1.91 wt.% and 2.39 wt.%, respectively) were enhanced

to 2.55 wt.% at 77 K and 1 bar [10]. However, the high gravimetric storage capacities at cryogenic temperatures for MOF fall down at $\sim$1 wt % at 298 K and 100 bar.

Although microporous materials consist of inorganic materials, a class of organic microporous polymers has attracted the interest of researchers for their "intrinsic microporosity" (PIM). The PIM class of materials is amorphous organic microporous materials resulting from repeated experiments on phthalocyanine material in the 1990s. A network of PIMs shows higher surface areas and hydrogen uptake compared to nonnetwork PIMs with an H_2 capacity ranging from 1.83 wt.% to 1.92 wt.% at 1 bar and 77 K and a greater uptake of 3.94 wt.% at higher pressure (10 bar) [11]. Therefore, PIMs have shown hydrogen uptake results comparable to that of inorganic and organic porous materials such as zeolites and MOFs and even carbon materials with similar surface areas.

The metal-organic coordination polymers (M-CP) with the large internal surface area are one of the promising materials; new M-CPs have been synthesized with different conformations, improved surface area, and pore size. Dual-metal manganese copper (MnCu) ferrocenyl $[C_{10}H_9Fe]$ coordination polymer microspheres with hollow structure have been synthesized, and an H_2 uptake of 3.12 wt.% at 163 K was reported.

15.3 Chemical Hydrides

The use of alternative fuels, especially in a liquid form, is one of the most attractive storage approaches since liquid fuels are unmatched in terms of transportability and energy density, and they can rely on existing infrastructure [12]. Chemical hydrides are materials that contain hydrogen bonded chemically. They are able to store a large amount of hydrogen, even if they are not rechargeable on board. In any case, due to a higher binding energy (190–290 kJ $\times$ mol^{-1}) than physisorbed hydrogen (4–15 kJ $\times$ mol^{-1}), these materials are preferred to another form of hydrogen storage. The chemical hydrides can be classified into different categories such as complex metal hydrides, nonmetal hydrides, and the most known metal hydrides.

15.3.1 Complex Metal Hydrides

The complex metal hydrides are materials that contain hydrogen atoms covalently bound with a polyatomic anion. They are usually bound to lithium [Li], magnesium [Mg], sodium [Na], calcium [Ca], or less commonly transition metals.

15.3.1.1 Amides and Imides

The amide/imide systems are considered very interesting for the onboard application due to the possibility to store about 6.5 wt.% of H_2 [13]. The most common materials are based on Li. However, these systems have several drawbacks, such as slow reaction kinetics, high hydrogen release temperature, and bad cycling stability. To

enhance the hydrogen storage property of these systems, many authors have mixed different additives to improve their properties; some of these have introduced potassium fluoride [KF] to a mixture of lithium amide-lithium hydride [$LiNH_2$ - LiH] improving the cyclic performance of about four times; others have reduced the onset temperature for the dehydrogenation from 403 to 353 K, by introducing magnesium borohydride [$Mg(BH_4)_2$] in $2LiNH_2$/magnesium hydride [MgH_2]. Zhang et al. [14] investigated the effect of doping iron(III) chloride [$FeCl_3$] in $LiNH_2$ - 2LiH. They found a shift to low temperature and a reduction of dehydrogenation energy due to the formation of a new solid cubic phase of lithium imide chloride. One of the problems of these materials is the ammonia [NH_3] generation during the decomposition, which is a poison for fuel cells; a different approach was investigated to solve this drawback. One of these was that the introduction of Li_3AlH_6 in $2LiNH_2$ - MgH_2 suppresses the NH_3 release and in addition improves the dehydrogenation kinetics at low temperature. Baricco et al. [15] studied a mixed lithium amide/magnesium hydride compound to realize a storage hydrogen system to be integrated with a high-temperature proton exchange membrane (HT-PEM) fuel cell stack. The tank was designed to feed the stack for 2 h. The integration was possible due to the relatively low temperature for hydrogen release of this material.

15.3.1.2 Alanates [$MeAlH_4$]

The alanates class of materials are based around aluminohydride in which the hydrogen evolution takes place upon contact with water. They are good candidates for hydrogen storage due to the high theoretical hydrogen storage capacity, about 10 wt.%, and mild pressure and temperature of work. The alanates desorb hydrogen through chemical decomposition, by the formation of a hexahydro-aluminate as intermediate. Unfortunately, they present a slow kinetics during hydrogen cycling, so many efforts have been made to synthesize mixed alanates with good kinetics and thermodynamic properties. The $NaAlH_4$ has attracted much interest for high H_2 storage capacity (up to 5 wt.%) and desirable operating pressure and temperature. Zhang et al. [16] used zirconium dioxide on carbon [ZrO_2/C] as a catalyst for the dehydrogenation and hydrogenation of $NaAlH_4$ and found a significant reduction in the operating temperature and improvement in the kinetics. Also, the introduction of niobium pentoxide [Nb_2O_5] and titanium(III) chloride [$TiCl_3$] in the sodium alanate produces a beneficial effect in terms of kinetics due to a modification of the crystallographic structure of the alanates. Similarly, Zou et al. [17] demonstrated that the titanium(IV) oxide [TiO_2] strongly affects the catalytic activity for the dehydrogenation of $NaAlH_4$ obtaining a dehydrogenation capacity of about 4 wt. % stable for more than ten cycles. The dehydrogenation capacity of $NaAlH_4$ was improved by the addition of only 3 mol % of nickel ferrite [$NiFe_2O_4$] permitting to reach a good cycle stability at 423 K. In addition to the $NaAlH_4$, other metal aluminohydrides (where Me represents metal cations around the tetrahedral [AlH_4] anions), such as potassium, $KAlH_4$; lithium, $LiAlH_4$; yttrium, $Y(AlH_4)_3$; and magnesium, $Mg(AlH_4)_2$, alanates, were studied [18].

15.3.1.3 Borohydrides [Me(BH$_4$)$_n$]

The borohydrides are promising materials for H$_2$ storage due to very high potential hydrogen contents up to 18 wt.%. Unfortunately, they are limited by the higher temperature of dehydrogenation. To overcome this problem, a possible way is to destabilize the materials by incorporating additives in the structure or by confining it into nanoporous structures. In the first case, different compounds such as lithium borate [Li$_3$BO$_3$] [19], niobium(V) fluoride [NbF$_5$], or scandium [Sc] were used to improve the sluggish kinetics or favor the reversibility of the re-hydrogenation process. Regarding the effect of the nano-confinement, many papers report the results on the entrapping of the borohydrides into aerogel carbon, in carbon nano-cages, or in graphitic nanosheets. Many papers demonstrate the real applicability of borohydrides as hydrogen storage system to feed a PEMFC. Li et al. [20] developed an on-demand hydrogen generation based on NaBH$_4$ able to continuously supply H$_2$ for a 3kW PEMFC.

15.3.2 Nonmetal Hydrides

The nonmetal hydrides are less common than metal hydrides and complex metal hydrides. However, since one of the metal hydrides' drawbacks is the high weight, the nonmetal hydrides have increased their popularity in the last period. They usually contain boron [B], carbon [C], nitrogen [N], and oxygen [O] that are very reactive and can interact with H$_2$.

15.3.2.1 Nitrogen Hydrides [N$_x$H$_y$]

Among nitro-hydrides, the most promising materials are ammonia and hydrazine [N$_2$H$_4$]. In particular, the ammonia presents two advantages: the high H$_2$ contents 17 wt.%, and the well-known production technology. The disadvantage of NH$_3$ is related to the high temperature required to release H$_2$. For this reason catalysts able to help the ammonia decomposition have been studied. The most common catalysts are ruthenium [Ru] supported on oxides such as alumina [Al$_2$O$_3$], nickel [Ni], or copper [Cu]. The hydrazine, containing 12 wt.% of H$_2$, reacts explosively with oxidizing agents but diluted in water or in inert gas is stable, and its reaction of decomposition is controllable by catalysts. The most common catalysts are Ni, palladium [Pd], and platinum [Pt] supported on graphene nanosheets [21], graphene oxide [C$_x$: O, where x = 2.1 − 2.9], and graphene doped with boron.

15.3.2.2 Boron and Nitrogen Hydrides

The most common amine-boranes (ammonia borane [NH$_3$BH$_3$], hydrazine borane [N$_2$H$_4$BH$_3$]) present very high hydrogen content, but their use is limited by slow kinetics and thermodynamic to release H$_2$. The H$_2$ release can occur by decomposition, with exothermic steps that require high temperature, or by a hydrolytic process that requires efficient catalysts to improve the sluggish kinetic. The ammonia

borane has a hydrogen capacity of about 19 wt.%; to improve the kinetics reaction, different supported catalysts are studied [22]. Similarly, the confinement of NH_3BH_3 in aerogel or mesoporous silica produces a beneficial effect due to the reduction of decomposition temperature [23]. Hydrazine borane has a gravimetric hydrogen storage capacity of 15 wt.%. It can release H_2 by hydrolysis using different catalysts [24] or by thermolysis. In the last case to facilitate the decomposition reaction, $N_2H_4BH_3$ is mixed with alkali metal hydrides such as LiH, NaH, and KH [25] or destabilized by using graphene nano-fibers.

15.3.3 Metal Hydrides [MeH$_x$]

The hydrogen absorption mechanism on metal hydrides occurs under certain temperature and pressure conditions due to strong interactions between the metal surface and the hydrogen molecule dissociation.

The kinetics of this process is much slower in comparison to the adsorption of molecular hydrogen in porous materials, but atomic hydrogen in metal hydrides binds via chemical bonds with an around ten times stronger enthalpy of formation. This fact implies that higher temperatures are required in order to break the bonds and remove absorbed hydrogen from the structure.

The chemical reaction of hydrogen and metal powder to form a metal hydride is given by the overall equation (15.1) where Me denotes any kind of metal or alloy able to absorb hydrogen (H_2), MeH the corresponding metal hydride, and ΔH the enthalpy of the reaction:

$$Me + xH_2 + \Delta H \leftrightarrow MeH_x(\Delta H < 0) \qquad (15.1)$$

It is a reversible process, and, according to the principle of Le Chatelier-Braun, a pressure increase shifts the equilibrium to the right (hydrogen is absorbed), whereas a temperature increase shifts it to the left [26]. A release of hydrogen (desorption) from the metal hydride is therefore possible by either reducing the hydrogen pressure (P) or increasing the temperature (T). As the hydrogen absorption is generally exothermic, the endothermic desorption tends to cool the metal powder.

The stability in desorption phase (dissociation P) of the metal hydride is one important issue for its applicability. Technically, pressure and temperature conditions of the metal-hydrogen reaction depend on the desired application and can be typically assumed as P $\approx$ 1 − 100 bar and T $\approx$ 240 − 750 K. Pure, low electronegative metals (so-called A-metals, e.g., Li, Na, K, cesium [Cs], Mg, Ca, lanthanum [La], Ti, or Zr) form stable hydrides with high dissociation T and/or low equilibrium P. Therefore only a few, e.g., Mg (at a desorption pressure of 1 bar temperature of 573 K), seem interesting for technical applications. More electronegative metals (so-called B-metals, e.g., Cu, Ni, Co, Fe, Mn, Cr, or molybdenum [Mo]) form unstable hydrides at relevant T and P. Van Vucht et al. [27] evaluated the possibility of alloying A- and B-metals to produce intermetallic compounds with practicable metal hydride phase stability.

The absorption and desorption characteristics of the metal hydride can be varied by partial substitution of alloy elements. Therefore, an adaptation of the metal hydride to the respective application is possible. A smaller particle size is advantageous because the surface area is increased and the diffusion distance for dissolved hydrogen in the metal hydride bulk is decreased.

As the density of the metal hydride is smaller than the density of the respective metal, a hydrogenation stresses the lattice and therefore collapses the brittle metal hydride bulk. For this reason, activation process during the first several absorptions (ab-) and desorption (de-) cycles have been carried out to reduce the particle size in the order of 1–20 μm [28, 29] depending on the metal hydride.

A commonly used method to characterize metal hydrides is the pressure-concentration isotherm (PCI) measurement. The hydrogen uptake is generally given as a storage capacity of the metal hydride, which is the ratio between the absorbed hydrogen mass and the metal mass (%).

The absorption pressure is always higher than desorption pressure because, during the formation of the hydride phase, the lattice is expanded up to 30%. The induced stresses and deformations lead to a consumption of free enthalpy and contribute to the pressure hysteresis [27]. The hysteresis is an important characteristic that determines the applicability of the alloy. Especially in sorption systems, a small as possible hysteresis is necessary to increase the efficiency of the system.

High reaction enthalpy, combined with high density and low thermal conductivity of metal hydride powders, complicates experimental investigations of metal-hydrogen systems under isothermal conditions. The hydrogen uptake of a metal hydride can be determined either on gravimetric or on volumetric measurements. The gravimetric method requires a high precision balance to observe the absorption and desorption, whereas the volumetric method is based on the mass conservation in a closed system with known volume. If the system is fully sealed, the hydrogen uptake is proportional to the measured pressure loss in the system. Both principles and their respective advantages are described and compared in detail in [27].

Wang et al. [30] divided the hydriding process into three separated steps and developed a single equation for:

1. Dissolution of hydrogen on the surface
2. Diffusion of hydrogen through the lattice
3. Phase transformation or nucleation and growth

Different A-/B-metal combinations were investigated, and the variety of the obtained intermetallic compounds can be summarized as follows [31]: $A_2B(Zr_2Cu$, Ti_2Pd, $Mg_2Ni)$, AB (LaNi, MgNi, TiFe, ZrCo), A_2B ($TiMn_2$, $CaNi_2$, gadolinium cobalt [$GdCo_2$], $ZrMn_2$, $ZrCr_2$,$TiCr_2$), and AB_5 ($LaNi_5$, YCo_5, europium nickel [$EuNi_5$], $CaNi_5$, $LaCo_5$). The most significant results were obtained for Mg_2Ni with a 10 wt.% H_2 uptake at 423–573 K at 25 bar and for $LaNi_5$ with 1.4 wt.% H_2 uptake at 298 K at 2 bar [32].
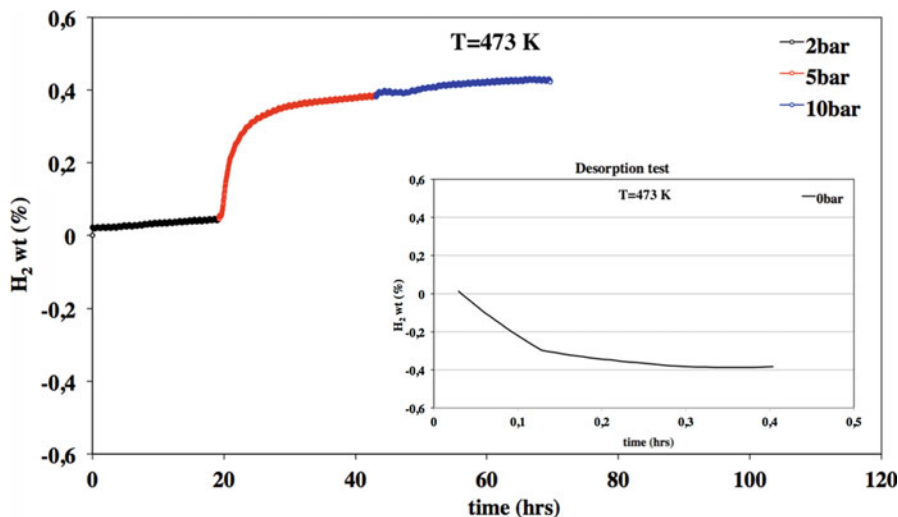
Fig. 15.1 Hydrogen sorption and desorption tests at 473 K

The formation of metal alloys before the hydride development is another approach. In this contest, Tuissi et al. [33] have proposed a new hydrogen storage Cr/Ti alloy. Pure metals Ti and Cr were melted by means of a vacuum arc furnace obtaining an atomic Cr/Ti ratio of 1.78:1.

The obtained Cr/Ti metal alloy, tested by using a Sievert apparatus type, has undergone a treatment before the test for activation, by repeatedly cycling P at different T. The kinetic of absorption reaction is influenced by the temperature with any H_2 sorption value at 298 K at 2 bar and 0.04 wt.% at 473 K in same P condition.

An interesting H_2 sorption trend (0.4 wt.%) is revealed at 5 bar, in which the kinetic reaction is faster than the other two pressures (Fig. 15.1). The reversibility of the process at the same temperature condition is verified, as reported in Fig. 15.1, and the total H_2 desorption is reached after about 20 min.

This hydrogen storage capacity is comparable to that of transition metals and/or rare earth alloy powders, commonly used for hydrogen storage applications at a temperature below 423 K, even if in this case the H_2 sorption measure was carried out at 473 K.

The interaction between alloy and hydrogen was confirmed by X-ray diffraction (XRD) spectroscopy. The XRD patterns of the material before and after H_2 absorption show diffraction signals shifted toward lower 2θ values, according to larger lattice parameters extracted from Rietveld refinements. On the basis of tabulated values for $TiCr_2$-based hydrates, the crystallographic cell dimensions should correspond to a rough composition $TiCr_2H_{0.4}$ [34].

15.4 Innovative Materials

15.4.1 Hybrid Materials

The reversibility of charge/discharge cycles in drastic conditions is a critical and fundamental aspect. The materials used for storage are subjected to strong mechanical stress that causes the collapse of structures.

For this reason, the attention is been addressed on polymeric composite materials even if only a few papers have been published about the use of synthetic polymers in this specific application. Moreover, the mechanical properties of the polymers damp down the mechanical stress that the embedded hydrogen storage material (e.g., a metal hydride) can undergo during sorption cycles, though there is still the open question whether the hosting polymer plays a role in modifying the hydrogen storage capacity of compounds like metal hydride. A possible explanation could be the interactions between hydrogen and the polymer chains and/or metal hydrides supported on these polymers. These interactions are generally a combination of covalent, ionic, metallic, H-bonds, and van der Waals [35]. Other important aspects that make polymer-based systems attractive for hydrogen storage are the low density and costs of the materials and the relative ease of synthesis, functionalization, and loading of the polymer matrix.

Some transition metal oxides, such as TiO_2 and manganese(IV) oxide [MnO_2], have been tested as dopants to improve the hydrogen sorption properties of light metals [36] and complex [37] hydrides and could possibly play a positive role for the interaction of the hydrogen also with the polymer matrix. Following these results, an alternative approach was taken by Pedicini et al. [38] to obtain a hybrid material based on a functionalized polymer containing a nanometric metal oxide.

A commercial polyether-ether-ketone (PEEK, [$(C_{19}H_{12}O_3)_m$-]) was selected as a matrix for its chemical-physical characteristics. A manganese oxide was linked onto a highly chlorosulfonated (100%[$SO_2(OH)Cl$]) PEEK to generate the sulfonated derivative $\left(\text{SPEEKCl-} \left[\left((CH_2)_3\text{-}\overset{\overset{\text{ci}}{|}}{\underset{\underset{\text{H}}{|}}{c}}\text{-}(CH_2)_3 \right)_n \text{--} \left(\overset{\overset{\text{H}}{|}}{\underset{\underset{\text{Cl\_SO}_2}{|}}{c}} \text{-} \right)_m \right] \text{-} \right)$ polymeric matrix as a metal compound able to promote the hydrogen storage. The chlorosulfonation of PEEK increases its surface area from 9.72 to 19.16 $m^2\,g^{-1}$ due to the introduction of chlorosulfonic groups, and the anchoring of the metal oxide does not change the surface area.

The manganese oxide was chosen as a hydrogen storage material for both its crystalline structure and its easy production method based on an in situ reaction.

Acting on precursor concentration potassium permanganate [$KMnO_4$], reaction time and temperature of several powders with the amount of Mn oxide ranging from 7 to 78 wt.% were obtained as shown in Table 15.1.

The variation of Mn oxide content, determined by different synthesis parameters conditions, is evidenced by the change in color and appearance of the powders

Table 15.1 SPMnO powder characteristics

Sample	[KMnO$_4$], mmoles	T, K	Time, h	Mn oxide, wt.%
SPMnO1	2	323	1	7
SPMnO2	3.2	323	1	13
SPMnO3	4	323	1	15
SPMnO4	4	323	3	20
SPMnO5	20	323	1	38
SPMnO6	20	323	3	78
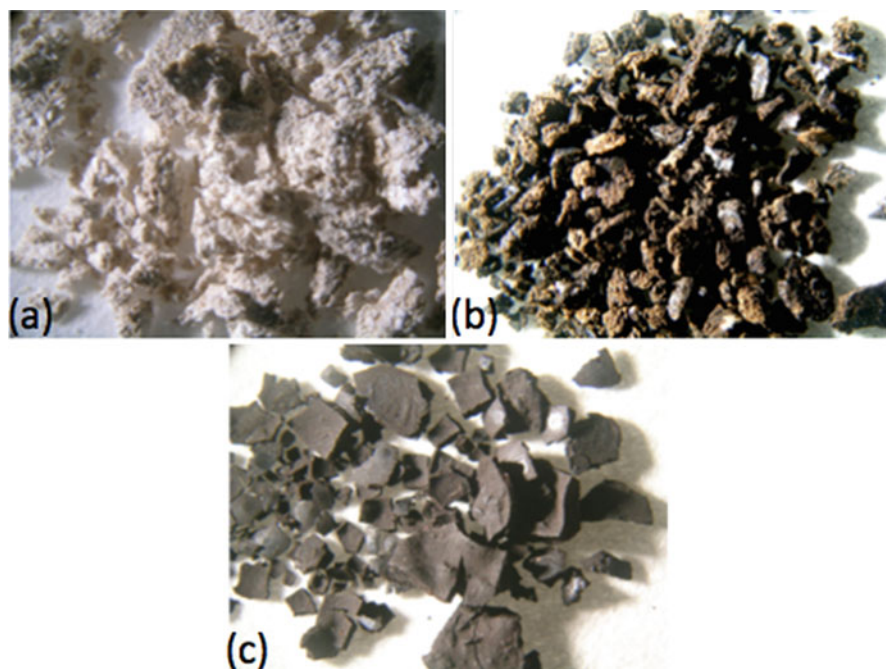
Fig. 15.2 SPMnO1 (**a**), SPMnO2 (**b**), and SPMnO6 (**c**) (Photos; reproduced with permission of Elsevier)

observed with an optical microscope. In Fig. 15.2, the photos relative to SPMnO1, SPMnO2, and SPMnO6 samples are shown.

The SPMnO1 sample (Fig. 15.2a), with the lowest percentage of manganese oxide (7 wt.%), shows spongy appearance and dirty white color very similar to the polymeric precursor as reported in [38]. Increasing the metal oxide content, the material tends to become darker and less spongy. When the amount is very high (78 wt.%, Fig. 15.2c), the predominance of the oxide is evident and the material becomes hard with the typical black color of Mn oxides.
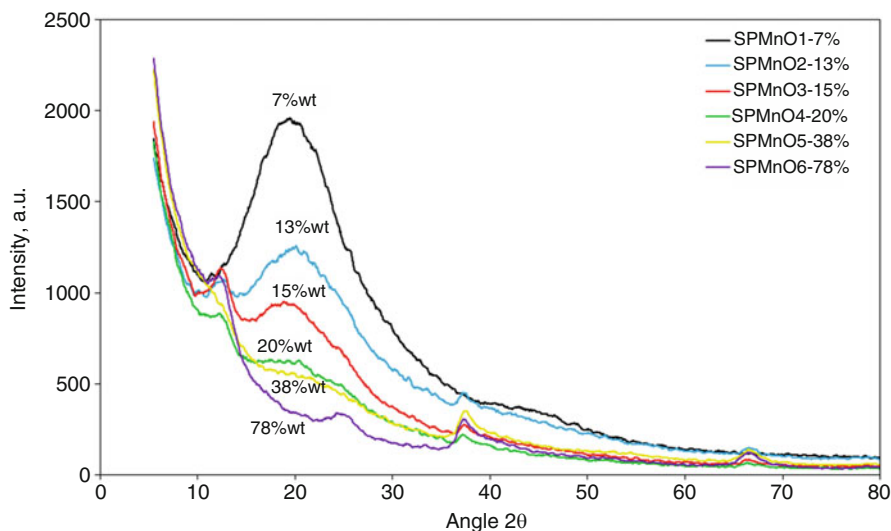
Fig. 15.3 SPMnO XRD comparison (Reproduced with permission of Elsevier)

The influence of the oxide amount on the structural properties of the prepared samples is evidenced by XRD profiles of all samples, as shown in Fig. 15.3. The peak centered at about 20° 2θ is due to the amorphous structure of the chlorosulfonated PEEK; this profile is maintained in all the developed samples and decreases by increasing the manganese oxide content and almost disappears in the SPMnO6 sample. All the samples present three characteristic peaks (12°, 37°, and 66° 2θ) of the layered manganese oxide of birnessite type. The crystal planes related to the birnessite structure, by following JCPDS data n° 05-673, have angles 12° 2θ{100}, 37° 2θ{003}Z, and 66° 2θ{005}Z.

Another peak at about 25° 2θ, particularly for the SPMnO5 and SPMnO6, is clearly visible and further confirms the structure of the oxide [39]. Furthermore, the oxide crystalline profile is not well defined as in pure oxide due to the presence of polymeric matrix.

To verify the possible H_2 sorption capability, three synthesized powders SPMnO3, SPMnO4, and SPMnO6 have been characterized by using a Sievert's type gas sorption analyzer. The tests have been performed at 323 K and 383 K. For each test a sequence of different steps of hydrogen pressure was used to charge the samples: in particular, in all tests, 10, 20, 40, and 60 bar of hydrogen pressure has been charged subsequently. Figure 15.4 shows the hydrogenation curves obtained for the three samples at 383 K. The maximum hydrogen uptake increases the manganese oxide content inside the sample.

Interestingly, for sample SPMnO3 (15 wt.%), the hydrogen saturation (0.10 wt.%) is reached with a hydrogen pressure (i.e., 40 bar) lower than that required for sample SPMnO4 (20 wt.%) for which H_2 sorption starts not before 60 bar with higher value of around 0.18 wt.%.
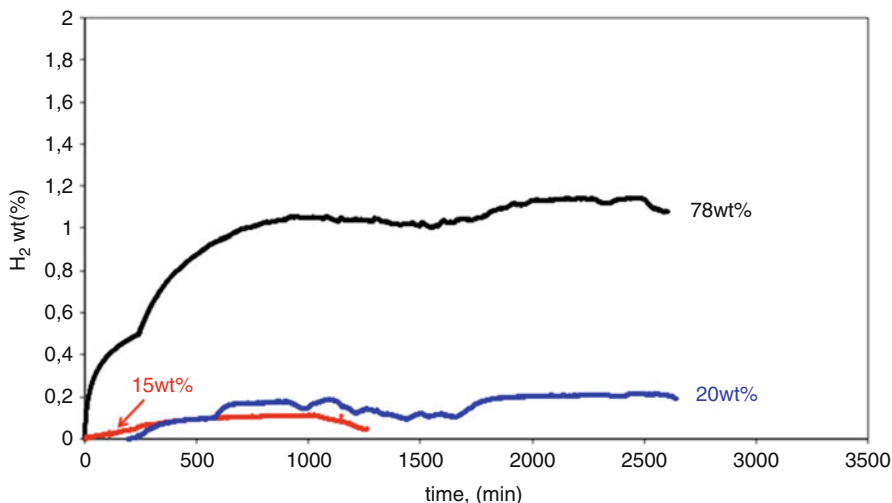
Fig. 15.4 SPMnO H_2 sorption comparison

A remarkable result was obtained for sample SPMnO6; the sample showed a high hydrogen capacity, compared to the other samples, already at 10 bar (0.5 wt.%). Once the system was approaching the saturation at 10 bar, a successive step was directly performed at 60 bar. Surprisingly, the sample was able to reach H_2 saturation more than after 1 wt.% after 1000 min, which is, up to now, a value never reached for polymer-based systems at no cryogenic conditions.

Encouraged by these promising results, the measurement temperature of this last sample was lowered at 323 K. The behavior is shown in Fig. 15.5a. The H_2 sorption does not reach the saturation in any P step, and the kinetic reaction is very slow. In any case, at 20 bar, the H_2 sorption is more than 1 wt.%, which is the highest value obtained at 383 K, while at 40 bar, the maximum H_2 sorption value was more than 3 wt.%. The reversibility of the H_2 sorption/desorption cycles was performed, at 323 K, with the aim of evaluating the stability of the material after sorption tests.

The limited number of sorption/desorption cycles was caused by technical reasons; anyway, reversible cycles were reached, and the previous H_2 sorption value at 20 bar was confirmed (in same time range). In addition, the short time of desorption process (5 min) was sufficient to evacuate H_2 completely since subsequent H_2 sorption steps are reproduced.

A further confirmation of the stability of the developed material after the volumetric test was obtained by XRD analysis, in which the profiles before and after test did not show substantial differences maintaining unaltered the crystallographic structure.

A modeling study by ab initio density functional theory (DFT) was carried out on this kind of material. A supercell, containing $2 \times 2 \times 3$ unit cells of MnO_2 and having 24 Mn and 48 O, was used. The hydrogen atoms were gradually placed in different locations inside the voids. For each number of H atoms, several
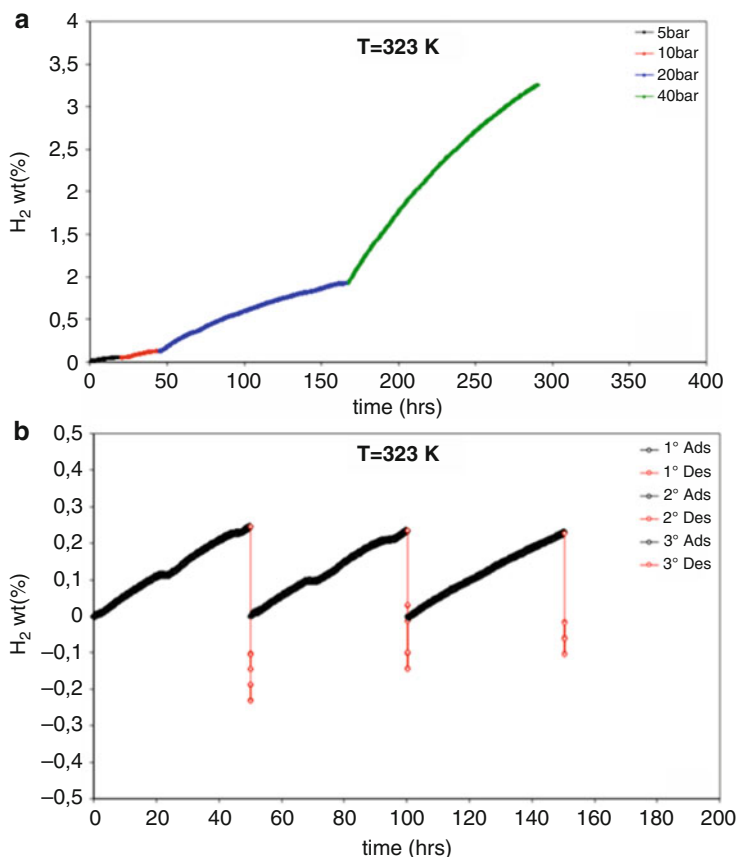
Fig. 15.5 (**a**) H_2 sorption test and (**b**) H_2 ads/des cycles of SPMnO6 (Reproduced with permission of Elsevier)

configurations were calculated (with H atoms in different locations) in order to find the one with the lowest energy. Figure 15.6 shows the lowest energy configurations with 6, 12, and 24 H atoms (b, c, and d, respectively).

The desorption energy was calculated with Eq. 15.2:

$$\Delta E = 2(E(Mn_{24}O_{48}) + n/2E(H_2) - E(Mn_{24}O_{48}H_n))/n \qquad (15.2)$$

The ΔE starts from the high value of about 365 kJ/mol for $n = 2$ and constantly drops to about 150 kJ mol^{-1} for $n = 36$. This starting value is higher than some metal hydrides, for instance, MgH about 100 kJ mol^{-1} or BeH about 240 kJ mol^{-1} [40].

Starting from the experimental H_2 sorption value (it was considered 1.7 wt.% instead of 3 wt.% really obtained), it was calculated the number of the respective H atoms corresponds to 36, with desorption energy value of 150 kJ mol^{-1}.

Fig. 15.6 The xy cross section of the lowest energy configurations for $Mn_{24}O_{48}H_n$ with n = 0, 6, 12, and 24 H atoms (**a**, **b**, **c**, and **d**, respectively). Mn, O, and H atoms are shown as blue, red, and white spheres, respectively (Reproduced with permission of Elsevier)
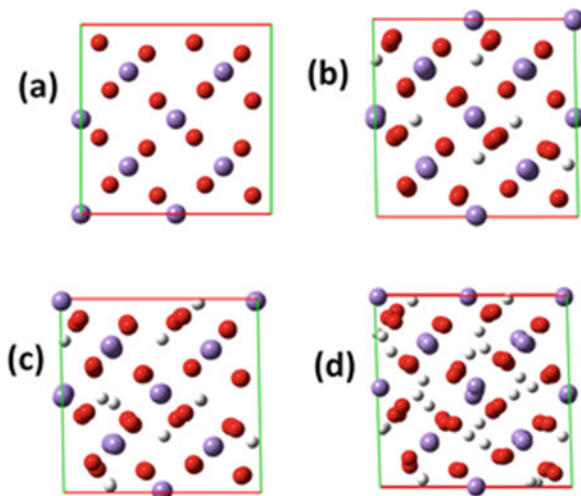

Table 15.2 SPMnO powder characteristics and H_2 storage values at 383 K/60 bar

Sample	[KMnO$_4$], mmoles	T, K	Time, h	Mn oxide, wt.%	H$_2$ sorption, wt.%
SPMnOC	30	353	1	83	0.62
SPMnOD	30	323	3	81	0.95
SPMnOE	12	368	1	78	0.97
SPMnOF	14.2	368	3	85	1.16

To verify the influence of Mn oxide amount on H_2 storage capacity, other samples were developed using more drastic preparative conditions to obtain loading over 78 wt.%. The maximum reachable value was 85 wt.%, but the corresponding H_2 sorption value was about 1 wt.% almost constant for any loading. These results are reported in Table 15.2.

Moreover, the samples obtained in such drastic operative conditions did not show any H_2 reversibility capacity. This behavior was confirmed by XRD postmortem analyses where a structural change was detected. A crystalline structure of the test corresponding to Mn_2O_3 was detected, meaning that the H_2 reacted with the oxide reducing Mn^{+4} to Mn^{+3}.

The encouraging results in terms of hydrogen absorption reached on sample SPMnO6 have promoted this material for application in a prototype tank; in fact, its lightweight and easy to handle render this material promising for real application.

An integrated small-scale system consisting of a hydrogen tank, having a capacity of 5–8 normal liters (NL) of hydrogen and a 25 cm^2 single polymer electrolyte fuel cell (PEFC), has been realized and tested to assess the performance of the innovative hydrogen storage material [41]. A precautionary H_2 sorption value of 1.1 wt.% (T = 383 K and P = 60 bar) was considered. Starting from these features, 20 g of material is necessary to feed a 25 cm^2 single cell, and the following parameters (Table 15.3) were considered to size the tank:

Table 15.3 Theoretical electrochemical parameters with 20 g of sample; reproduced from [42] with permission of Elsevier

Parameter	Amount	Units
H_2 stoichiometry	1	–
Composite material amount	20	g
Absorption ratio	1	% mass
Absorbed H_2	0.20	g
PM H_2	2	g mol^{-1}
Absorbed H_2 moles	0.10	mol
Constant molar volume	22.41	NL mol^{-1}
Absorbed H_2 volume	2.24	NL
H_2 volume at 50 bar	0.04	L
Single-cell active area	25	cm^2
Specific power	400	mW cm^{-2}
Single-cell power	10	W
Cell potential	0.60	V
Cell current	16.67	A
H_2 consumed	8.636E-05	mol s^{-1}
Lifetime	1158	s
Lifetime	19.30	min

The lifetime of the test was calculated from the molar consumption of reagents (Faraday's law) of the cell at the fixed current, while the potential was chosen to compare the data with other tests performed in a fuel test station. From this data sheet, the cylinder has an H_2 molar volume of 2.24 NL, able to feed a 25 cm^2 single cell with a 400 mW cm^{-2} power density at 0.6 V, corresponding a total power of 10 W.

The prototype tank before and after the loading of the material is shown in Fig. 15.7.

Two types of test were performed to measure the performance of the small tank. The first test includes the measurement of the quantity of gas released by the tank. The tests were performed at two constant flow rates, 100 mL min^{-1} and 200 mL min^{-1}. After each test, the hydrogen tank was recharged at 60 bar (g) and 383 K and different recharge time. The recharge time is recorded to understand the most convenient value relative to desorption performance. A total of six tests have been performed and their results summarized in Table 15.4. The net discharge time was considered taking into account the dead volume related to piping and connections.

Test results show a pretty constant performance in terms of gas output. The average duration of the gas flow is approximately 15 min at a flow rate of 200 mL min^{-1} (tests n. 4–6) and 23 min at 100 mL min^{-1} (tests n. 1–3).

The discharge time versus charge time is then plotted to highlight their correlation (i.e., the tendency to a plateau which shows the end of the absorption process) and any possible anomaly (i.e., significant gas leakage) (Fig. 15.8). As shown in Fig. 15.8, an increase of charge time did neither lead to a proportional increase nor a constant value of discharge time; the adsorption process requires a longer time than the desorption process.
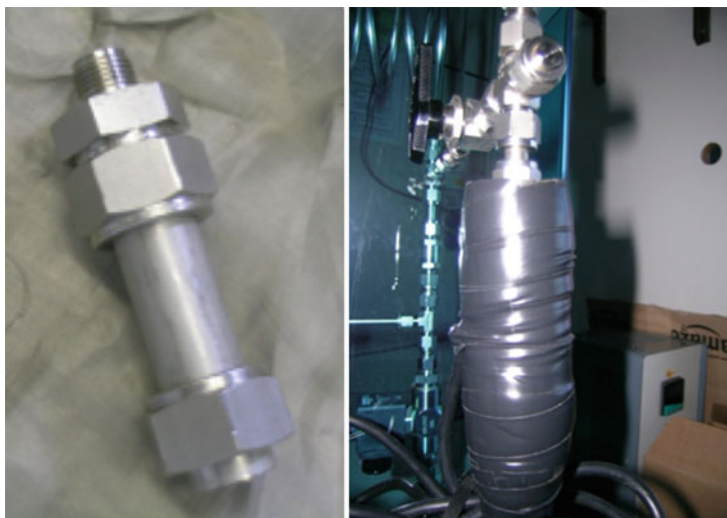
Fig. 15.7 Prototype tank (Reproduced from [42] with permission of Elsevier)

Table 15.4 Experimental data for charge/discharge of prototype tank

Test	Charge, min	Net discharge time, min	Flow, mL min^{-1}
1	30	9	100
2	120	19	100
3	420	21	100
4	60	7	200
5	120	11	200
6	220	8	200

Successively, the prototype tank was connected to a 25 cm^2 (active area) single cell operating in dead-end mode, so that the hydrogen desorption and the consumption rate can be theoretically estimated by using Faraday's law and measuring the current of the fuel cell. The single cell was previously tested at 353 K and 100% *RH* by supplying air and H$_2$ from the laboratory pipeline, to obtain the performance baseline. Figure 15.9a shows a comparison between the baseline fuel cell performance (blue line) and the electrochemical test, performed with the actual system (green line). The two curves were obtained under the same operative conditions at 353 K 1.5 bar and 0.6 V fixed potential, but dry hydrogen was used to feed anode side in the prototype configuration. Unstable behavior was recorded under potentiostatic condition because, in this case, the mass flow controller must manage the flow according to any current fluctuation, leading to flow instability.

The same comparison was carried out at fixed current as shown in Fig. 15.9b. The different performance of the PEFC single cell (blue line vs. green line) is related to the different operative conditions when the cell is fed with the hydrogen from the pipeline (3 bar, 353 K, fully humidified hydrogen, 2.5 stoichiometric at 15 A) or
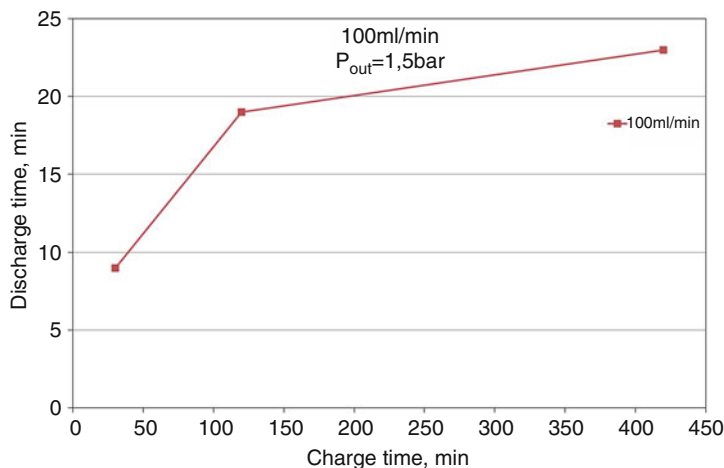
Fig. 15.8 Discharge versus charge time at 100 mL min−1; (Reproduced from [42] with permission of Elsevier)

from the tank (353 K, 1.5 bar, dry H_2, stoichiometric value at 10 A). In the galvanostatic test, a more stable behavior was recorded because the gas consumption rate is constant; hence the mass flow controller follows the set point.

The test lasted 10 min instead of the foreseen discharge time of 20 min due to the hydrogen leakage that reduced the tank autonomy.

As shown in Fig. 15.9b, the fuel cell performances of the prototype system are comparable to that laboratory system when appropriate test conditions were used. Therefore, the innovative material could be used for practical applications with further improvement in terms of material storage capacity and system design.

15.4.2 Natural Material

Due to the large variety of elements present in natural volcanic powders [42], this material was taken into consideration for a possible application in hydrogen storage. Two different volcanic samples were analyzed for this study. The first sample (sample red) is coming from an 1892 Etna Vulcan eruption showing oxidized metals, due to a long exposition to the atmospheric agents. The second sample (sample gray) is a lava rock, sampled during a 2006 summit eruption, and was not contaminated by the atmospheric agents. Both of these samples show phenocryst assemblage, which is common to most Etnean volcanics. From X-ray fluorescence spectrometer analyses, the following composition was revealed: <1% for silicon(IV) oxide [SiO_2], TiO_2, Al_2O_3, MnO, total Fe in $Fe_2O_3^{(tot)}$, MgO, CaO, and K_2O; <5% sodium oxide [Na_2O] and phosphorus(V) oxide [P_2O_5]; and between 5% and 10% for all trace elements. From volumetric analyses, sample red has shown a hydrogen storage
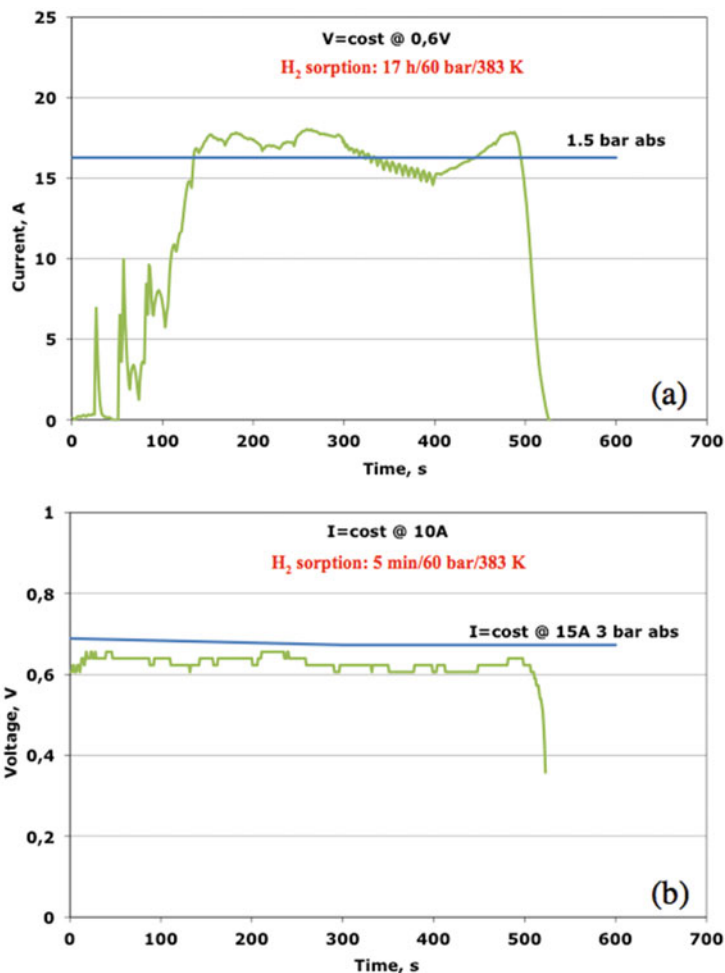
Fig. 15.9 Comparison of fuel cell performance at fixed potential (**a**) and current (**b**) by using standard and prototype H_2 feeding (Reproduced from [42] with permission of Elsevier)

capability of about 2.5 wt.% at 303 K and 40 bar, while sample gray has supplied a higher capability reaching a value of about 4 wt.% in the same operative conditions (Fig. 15.10).

This value was obtained after 280 h; on the contrary, the first sample, at the same time, stores about one-half of H_2, meaning that the hydrogen sorption kinetic of sample gray is faster than sample red. This wide difference could be attributable to different factors such as high purity of sample gray, not polluted by the atmospheric agents and smaller and homogeneously dispersed particles. From a structural
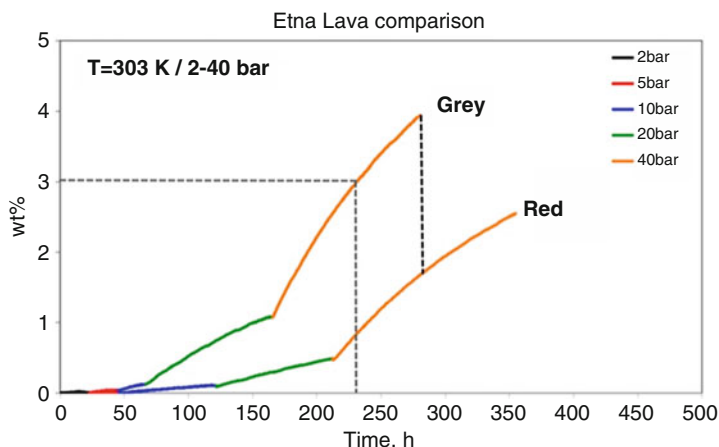
Fig. 15.10 Comparison of hydrogen sorption

postmortem characterization by XRD was verified that the hydrogen sorption tests do not produce any modification in the structure of the materials. In conclusion, good and promising results were obtained using natural samples based on volcanic rocks in very mild conditions.

15.5 Conclusions

The need to use hydrogen as a carrier for energy has pushed the research toward the study of hydrogen storage with the aim to find available solid-state materials that have suitable requisites for the use in mobile applications. Several classes of materials have been investigated based on H_2 physisorption (carbonaceous, high surface area (HSA) materials) and chemisorption (complex metal hydride, metal hydrides). Generally, all these materials present high H_2 sorption capacity in cryogenic conditions not fully satisfactory for real application. For this reason, the interest toward innovative materials is increased. Recently, a hybrid material based on a functionalized polymer (PEEK) containing different percentages of nanometric Mn oxides was investigated. The XRD patterns highlighted that the developed manganese oxide presents the fundamental peaks of MnO_2 corresponding to lamellar birnessite structure. A low amount of Mn oxide (15 wt.%) and H_2 sorption of 1.2 wt.% was obtained in cryogenic conditions (77 K at 1 bar). Very promising results were reached in mild conditions when a load of 80 wt.% Mn oxides were used. From Sievert apparatus, H_2 sorption values of 3 wt.% at 323 K at 40 bar and 1.1 wt.% at 383 K and 60 bar were obtained.

Furthermore, by short H_2 sorption/desorption cycles, a total reversibility was demonstrated. These results made possible the application of this material in a prototype tank integrated to a polymer electrolyte single cell. The results were comparable to those obtained in a laboratory system. Through a modeling study,

ab initio density functional theory, a desorption energy value comparable to metal hydrides was found, supporting the results obtained in this study.

Among innovative materials, natural volcanic powders coming from Etna Vulcan eruptions were investigated. These materials, containing a large variety of elements, could promote the H_2 sorption. From preliminary H_2 sorption tests, an H_2 uptake of about 4 wt.% at 303 K and 40 bar was recorded on a summit lava rock coming from the 2006 eruption. Despite the significant advances in solid-state material for H_2 storage and many encouraging results, extensive research in this field is in constant evolution.

References

 1. S. Borowitz, *Farewell Fossil Fuels*, Springer Science book ISBN 978-0-306 45781-4, (1999)
 2. http://www.fch.europa.eu/page/multi-annual-work-plan
 3. S. Iijima, Nature **354**, 56 (1991); A.C. Dillon, K.M. Jones, T.A. Bekke-dahl, H. Kiang, D.S. Bethune, M.J. Heben, Storage of hydrogen in single-walled carbon nanotubes. Nature **386**, 377–379 (1997)
 4. E. Poirier, R. Chahine, T.K. Bose, Int. J. Hydrog. Energy **26**, 831 (2001)
 5. H. Wang, Q. Gao, J. Hu, High hydrogen storage capacity of porous carbons prepared by using activated carbon. J. Am. Chem. Soc. **131**, 7016–7022 (2009)
 6. Z. Wang, L. Sun, F. Xu, H. Zhou, X. Peng, D. Sun, J. Wang, Y. Du, Nitrogen-doped porous carbons with high performance for hydrogen storage. Int. J. Hydrogen Energy **41**, 8489–8497 (2016)
 7. H. Jung, K.T. Park, M.N. Gueye, S.H. So, C.R. Park, Bio-inspired graphene foam decorated with Pt nanoparticles for hydrogen storage at room temperature. Int. J. Hydrogen Energy **41**, 5019–5027 (2016)
 8. N.L. Rosi, J. Eckert, M. Eddaoudi, D.T. Vodak, J. Kim, M. O'Keeffe, O.M. Yaghi, Hydrogen storage in microporous metal-organic frameworks. Science **300**, 1127–1129 (2003)
 9. K. Koh, A.G. Wong-Foy, A.J. Matzger, A porous coordination copolymer with over 5000 m^2/g BET surface area. J. Am. Chem. Soc. **131**, 4184–4185 (2009)
10. N.M. Musyoka, J. Ren, P. Annamalai, H.W. Langmi, B.C. North, M. Mathe, D. Bessarabov, Synthesis of a hybrid MIL-101(Cr)/ZTC composite for hydrogen storage applications. Res. Chem. Intermed. **42**, 5299–5307 (2016)
11. D. Ramimoghadam, E. MacA Gray, C.J. Webb, Review of polymers of intrinsic microporosity for hydrogen storage applications. Int. J. Hydrogen Energy **41**, 16944–16965 (2016)
12. O. Elishav, D.R. Lewin, G.E. Shter, G.S. Grader, The nitrogen economy: economic conomic feasibility analysis of nitrogen-based fuels as energy carriers. Appl. Energy **185**, 183–188 (2017). https://doi.org/10.1016/j.apenergy.2016.10.088
13. P.L. Bramwell, S. Lentink, P. Ngene, P.E. De Jongh, Effect of pore confinement of $LiNH_2$ on ammonia decomposition catalysis and the storage of hydrogen and ammonia. J. Phys. Chem. C **120**(48), 27212–27220 (2016). https://doi.org/10.1021/acs.jpcc.6b10688

14. Y.Z. Ge, W.Y. Ye, Z.H. Shah, X.J. Lin, R.W. Lu, S.F. Zhang, PtNi/NiO clusters coated by hollow silica: novel design for highly efficient hydrogen production from ammonia-borane. ACS Appl. Mater. Interfaces **9**(4), 3749–3756 (2017). https://doi.org/10.1021/acsami.6b15020

15. M. Baricco, M. Bang, M. Fichtner, B. Hauback, M. Linder, C. Luetto, P. Moretto, M. Sgroi, SSH2S: Hydrogen storage in complex hydrides for an auxiliary power unit based on high-temperature proton exchange membrane fuel cells. J. Power Sources **342**, 853–860 (2017). https://doi.org/10.1016/j.jpowsour.2016.12.107

16. X. Zhang, R.Y. Wu, Z.Y. Wang, M.X. Gao, H.G. Pan, Y.F. Liu, Preparation and catalytic activity of a novel nanocrystalline ZrO_2@C composite for hydrogen storage in $NaAlH_4$. Chem-Asian J **11**(24), 3541–3549 (2016). https://doi.org/10.1002/asia.201601204

17. G. Zou, B. Liu, J. Guo, Q. Zhang, C. Fernandez, Q. Peng, Synthesis of nanoflower-shaped MXene derivative with unexpected catalytic activity for dehydrogenation of sodium Alanates. ACS Appl. Mater. Interfaces **9**(8), 7611–7618 (2017). https://doi.org/10.1021/acsami.6b13973

18. J.R. Ares, J. Zhang, T. Charpentier, F. Cuevas, M. Latroche, Asymmetric reaction paths and hydrogen sorption mechanism in mechanochemically synthesized potassium alanate (KAlH4). J. Phys. Chem. C **120**(38), 21299–21308 (2016). https://doi.org/10.1021/acs.jpcc.6b07589

19. Y.F. Ma, Y. Li, T. Liu, X. Zhao, L. Zhang, S.M. Han, Y.J. Wang, Enhanced hydrogen storage properties of LiBH4 generated using a porous Li_3BO_3 catalyst. J. Alloys Compd. **689**, 187–191 (2016). https://doi.org/10.1016/j.jallcom.2016.07.313

20. S.C. Li, F.C. Wang, The development of a sodium borohydride hydrogen generation system for proton exchange membrane fuel cell. Int. J. Hydrog. Energy **41**(4), 3038–3051 (2016). https://doi.org/10.1016/j.ijhydene.2015.12.019

21. D. Lu, G.F. Yu, Y. Li, M.H. Chen, Y.X. Pan, L.Q. Zhou, K.Z. Yang, X. Xiong, P. Wu, Q.H. Xia, RuCo NPs supported on MIL-96(Al) as highly active catalysts for the hydrolysis of ammonia borane. J. Alloys Compd. **694**, 662–671 (2017). https://doi.org/10.1016/j.jallcom.2016.10.055

22. L.M. Zhou, J. Meng, P. Li, Z.L. Tao, L.Q. Mai, J. Chen, Ultrasmall cobalt nanoparticles supported on nitrogen-doped porous carbon nanowires for hydrogen evolution from ammonia borane. Mater. Horiz. **4**(2), 268–273 (2017). https://doi.org/10.1039/c6mh00534a

23. M. Rueda, L.M. Sanz-Moral, J.S.B. Jose, A. Martin, Improvement of the kinetics of hydrogen release from ammonia borane confined in silica aerogel. Microporous Mesoporous Mater. **237**, 189–200 (2017). https://doi.org/10.1016/j.micromeso.2016.09.030

24. Z.J. Zhang, Y.Q. Wang, X.S. Chen, Z.H. Lu, Facile synthesis of NiPt-CeO_2 nanocomposite as an efficient catalyst for hydrogen generation from hydrazine borane. J. Power Sources **291**, 14–19 (2015). https://doi.org/10.1016/j.jpowsour.2015.05.012

25. R. Moury, K. Robeyns, Y. Filinchuk, P. Miele, U.B. Demirci, In situ thermodiffraction to monitor synthesis and thermolysis of hydrazine borane-based materials. J. Alloys Compd. **659**, 210–216 (2016). https://doi.org/10.1016/j.jallcom.2015.11.052

26. P. Chen, E. Akiba, S. Orimo, A. Zuettel, L. Schlapbach, Hydrogen storage by reversible metal hydride formation in the *Book: Hydrogen Science and Engineering: Materials, Processes, Systems and Technology* (2016)

27. G. Friedlmeier, M. Groll, Experimental analysis and modeling of the hydriding kinetics of Ni-doped and pure Mg. J. Alloy Compd, Elsevier-Amsterdam, **253–254**, 550–555 (1997)

28. H. Wang, H.J. Lin, W.T. Cai, L.Z. Ouyang, M. Zhu, Tuning kinetics and thermodynamics of hydrogen storage in light metal element based systems – a review of recent progress. J. Alloys Compd. **658**, 280–300 (2016)

29. M. Ron, The normalized pressure dependence method for the evaluation of kinetic rates of metal hydride formation/decomposition. J. Alloy Compd. **283**, 178–191 (1999)

30. C.S. Wang, X.H. Wang, Y.Q. Lei, C.P. Chen, Q.D. Wang, The hydriding kinetics of MlNi5 – I. Development of the model. Int. J. Hydrogen Energy **21**, 471–478 (1996)

31. J. Yang, A. Sudik, C. Wolverton, D.J. Siegel, High capacity hydrogen storage materials: attributes for automotive applications and techniques for materials discovery. Chem. Soc. Rev. **39**, 656–675 (2010)

32. K. Sanjay, H. Miyaoka, T. Ichikawa, G.K. Dey, Y. Kojima, Micro-alloyed Mg2Ni for better performance as negative electrode of Ni-MH battery and hydrogen storage. Int. J. Hydrog. Energy **42**, 5220–5226 (2017)
33. R. Pedicini, I. Gatto, M. Coduri, C.A. Biffi, A. Tuissi, Preliminary investigation on metal alloy based on Cr/Ti, HYPOTHESIS XII Conference, Syracuse, 28–30 June 2017
34. H. Imoto, M. Sasaki, T. Saito, Y. Sasaki, Bull. Chem. Soc. Jpn. **53**(6), 1584–1587 (1980)
35. W.R. Schmidt, Activity report of the United Technologies Research Center for the Polymer Dispersed Metal Hydride program, DOE contract DEFC36-00G010535
36. Z. Liu, Z. Lei, Cyclic hydrogen storage properties of Mg milled with nickel nano-powders and MnO2. J. Alloys Compd. **443**, 121–124 (2007)
37. Y. Suttisawat, P. Rangsunvigit, B. Kitiyanan, S. Kulprathipanja, Effect of co-dopants on hydrogen desorption/absorption of $HfCl_4$- and TiO_2- doped $NaAlH_4$. Int. J. Hydrog. Energy **33**, 6195–6200 (2008)
38. R. Pedicini, A. Saccà, A. Carbone, E. Passalacqua, Hydrogen storage based on the polymeric material. Int. J. Hydrog. Energy **36**, 9062–9068 (2011)
39. G. Zhu, H. Li, L. Deng, Z.H. Liu, Low-temperature synthesis of δ-MnO_2 with large surface area and its capacitance. Mater. Lett. **64**, 1763–1765 (2010)
40. A.D. Zdetsis, M.M. Sigalas, E.N. Koukarasad, Phys. Chem. Chem. Phys. **16**, 14172–14182 (2014)
41. R. Pedicini, F. Matera, G. Giacoppo, I. Gatto, E. Passalacqua, Int. J. Hydrogen Energy **40**, 17388–17393 (2015)
42. R. Pedicini, L. Miraglia, A. Carbone, E. Passalacqua, I. Gatto, Interesting hydrogen storage behavior of volcanic powders, The III Energy & Materials Research Conference – EMR 2017 Lisbon, 5–7 Apr 2017
43. L. Miraglia, Tech. Report INGV **261**, 5–24 (2013)